THEORETICAL PREDICTIONS OF X-RAY AND EXTREME-UV FLARE EMISSIONS USING A LOSS-OF-EQUILIBRIUM MODEL OF SOLAR ERUPTIONS

KATHARINE K. REEVES

Smithsonian Astrophysical Observatory, 60 Garden Street, MS 58, Cambridge, MA 02138; kreeves@cfa.harvard.edu

HARRY P. WARREN

E. O. Hulburt Center for Space Research, Code 7670, Naval Research Laboratory, Washington, DC 20375

AND

TERRY G. FORBES

Institute for the Study of Earth, Oceans, and Space (EOS), University of New Hampshire, 39 College Road, Durham, NH 03824

ABSTRACT

In this paper, we present numerical simulations of solar flares that couple a loss-of-equilibrium solar eruption model with a one-dimensional hydrodynamic model. In these calculations, the eruption is initiated by footpoint motions that disrupt the balance of forces acting on a flux rope. After the eruption begins, a current sheet forms and an arcade of flare loops is created by reconnecting magnetic fields. Thermal energy input into the flare loops is found by assuming the complete thermalization of the Poynting flux swept into the current sheet. This thermal energy is input into a one-dimensional hydrodynamic code for each loop formed in the multithreaded flare arcade. We find that a density enhancement occurs at the loop top when the two evaporating plasma fronts in each leg of the loop collide there. Simulated flare images show that these loop-top density enhancements produce "bars" of bright emission similar to those observed in the *Transition Region and Coronal Explorer* (*TRACE*) 195 Å bandpass and loop-top "knots" of bright emission seen in flare observations by the Soft X-Ray Telescope (SXT) on *Yohkoh*. We also simulate flare spectra from the Bragg Crystal Spectrometer (BCS) on *Yohkoh*. We find that during the early stages of flare initiation, there are significant blueshifts in the Ca XIX line, but the intensities are too faint to be observed with BCS. In general, the results of this model simulate observed flare emissions quite well, indicating that the reconnection model of solar flares is energetically consistent with observations.

Subject headings: Sun: coronal mass ejections (CMEs) — Sun: flares

1. INTRODUCTION

The prevailing model of solar flares states that the energy release comes from the reconnection of oppositely directed magnetic field lines in the corona. The energy released during this reconnection event is transported to the chromosphere, either through thermal conduction (e.g., Forbes & Acton 1996) or precipitation of energetic particles (e.g., Lin & Hudson 1976). The chromosphere is heated, which causes the evaporation of material from the chromosphere into the corona, resulting in flare loops filled with dense, hot plasma.

One-dimensional hydrodynamic calculations have been used for many years to simulate energy deposition and chromospheric evaporation in flare loops (e.g., Cheng et al. 1983; Doschek et al. 1983; Fisher et al. 1985b; Mariska 1987). These models have been successful in predicting the high temperatures and densities observed in flares. However, they also predict upflowing plasma velocities that should result in large blueshifts in spatially unresolved spectral flare observations that are typically not seen. Full-Sun spectra gathered at the time of flare onset are generally dominated by centroid emission due to stationary plasma, which is only sometimes accompanied by a lower intensity blueshifted component (Antonucci et al. 1990; Doschek et al. 1994). In the rare cases where a strong blueshift is observed, it is correlated with the release of hard X-rays, indicating that an impulsive energy source could be responsible for both phenomena (Bentley et al. 1994).

One possible solution to the discrepancy between the one-dimensional numerical simulations and observations is the idea that flares are made up of many loops, or threads, that are being energized at different times, and all contribute to the observed emission. Observational support for this idea comes from spatially resolved spectral observations such as those from the Coronal Diagnostic Spectrometer (CDS) on the *Solar and Heliospheric Observatory* (*SOHO*). These observations provide evidence for localized blueshifts near the flare ribbons (Milligan et al. 2006; Brosius & Phillips 2004; Czaykowska et al. 1999), indicating that only the threads in the vicinity of the ribbons (and hence the reconnection site) are experiencing chromospheric evaporation.

Calculations using multiple one-dimensional hydrodynamic simulations have previously been used to calculate flare emissions (Hori et al. 1997, 1998; Reeves & Warren 2002; Warren & Doschek 2005; Warren 2006). These simulations have been able to reproduce X-ray and spectral observations of flares, but they have either used empirical energy inputs derived from data from *The Geostationary Operational Environmental Satellite* (*GOES*; Warren & Doschek 2005; Warren 2006), or arbitrary heating functions specifically tailored to match the observations (Hori et al. 1997, 1998; Reeves & Warren 2002). In this paper, we take a different approach and calculate the heat generated in each strand in a multithreaded flare arcade using a model of the reconnection process. Since we calculate the heat input from the reconnection physics, we can then simulate observations to test if the reconnection model of solar flares is energetically consistent with observed flare emissions.

We model the flare reconnection process using the loss-of-equilibrium model developed in Reeves & Forbes (2005a). The thermal energy output from this model is then used as the input
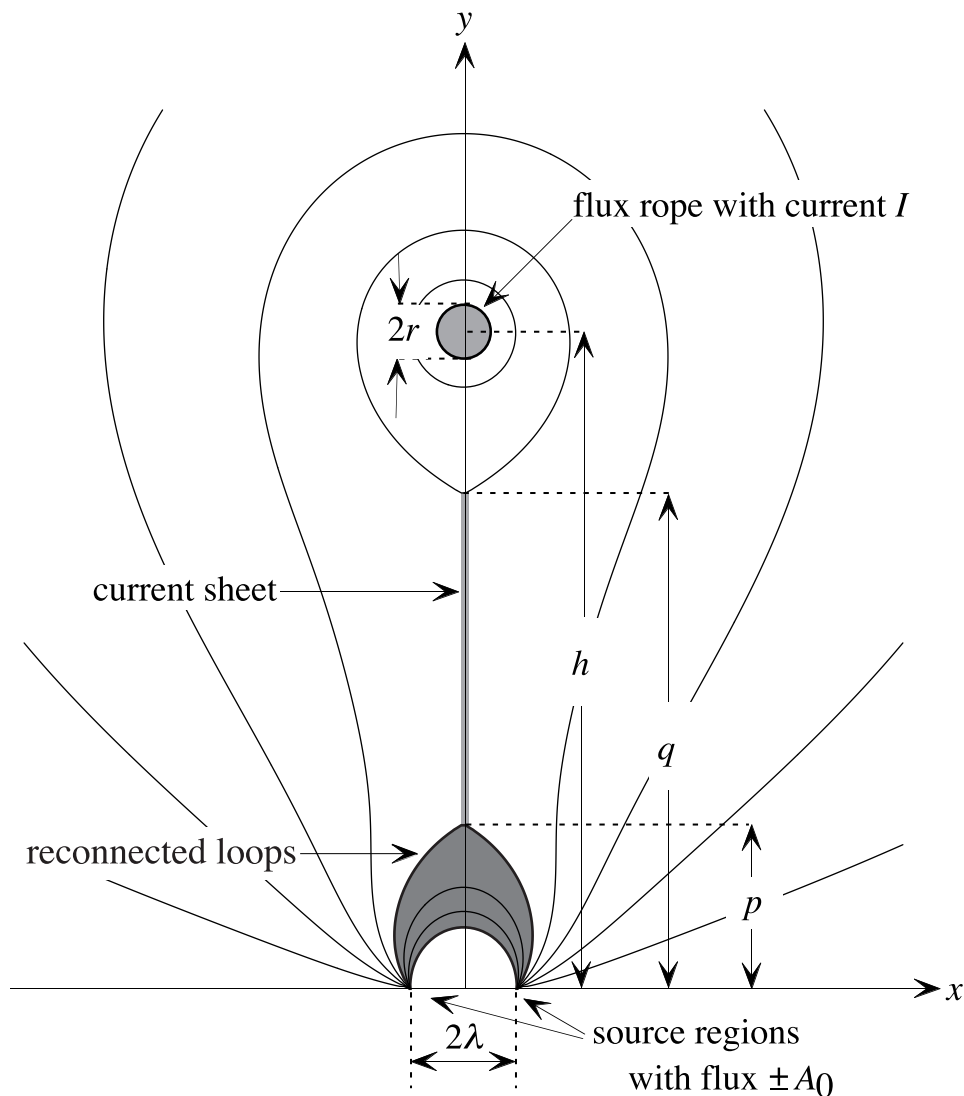
Fɪɢ. 1.—Magnetic configuration for the loss-of-equilibrium model after the initiation of the eruption and the formation of the current sheet. From Reeves & Forbes (2005a).

into our multithreaded hydrodynamic loop flare simulation. In the loss-of-equilibrium model, the eruption is caused by an unbalancing of the magnetic tension and compression forces acting on a flux rope suspended in the corona. After the eruption, a vertical current sheet forms blow the ejected flux rope, and reconnection in this sheet causes an arcade of flare loops to form. In this paper, we assume that there is complete thermalization of the Poynting flux swept into a current sheet above the flare loop system, although in practice, we expect some of the energy, perhaps less than 10%, to be transferred to the kinetic energy of the flux rope. We also assume that half of this thermal energy is directed into the flare loops, while the other half is directed upward toward the flux rope. The thermal energy directed into the flare loops is then assumed to be the heat source for a one-dimensional hydrodynamic model of each loop in the arcade.

In a previous version of this model, we found that the thermal energy dissipated in the current sheet gives rise to flare light curves characteristic of observations (Reeves & Forbes 2005a). For those calculations, a simplified plasma cooling model was employed to calculate the temperatures and densities in the flare loops. This method is computationally efficient, but it does not provide plasma velocities or spatial resolution within the flare loops. In this paper, we use a full hydrodynamic code to calculate the plasma param-

eters in the flare loops, allowing us to calculate plasma velocities needed to simulate flare spectra and glean spatial information about the plasma in the flaring loops.

In § 2 we discuss the details of the loss-of-equilibrium model. In § 3 we discuss the details of the hydrodynamic loop code. Flare light curves and images are presented in § 4, and flare spectra are calculated in § 5. The summary and conclusions are presented in § 6.

2. LOSS-OF-EQUILIBRIUM FLARE INITIATION MODEL

The model we use for the flare initiation is based on a version of the Lin & Forbes (2000) model that has been expanded to include gravity (Lin 2004; Reeves & Forbes 2005b). In this model, a flux rope is held in equilibrium prior to eruption by a balance among the gravitational force, the magnetic tension force, and the magnetic compression force. The compression force arises from the field squeezed between the flux rope and the Sun's surface, while the tension force arises from an overlying arcade field produced by two localized sources of opposite polarity at the Sun's surface. As these surface sources are quasi-statically brought closer together, a loss of equilibrium may occur and lead to an eruption. After the initiation of the eruption, a current sheet forms underneath the flux rope, as shown in Figure 1. The current sheet is

detached from the solar surface, allowing an arcade of reconnected magnetic loops to form between the localized sources as the eruption progresses.

In this paper, we expand on the previous study of Reeves & Forbes (2005a) by incorporating a one-dimensional flare code to calculate density, temperature, and velocity along each individual field line in the flare loop system. With this addition, we can calculate flare spectra (excluding chromospheric lines) and construct two-dimensional synthetic images of the flare loop system as a function of time. We also include the gravitational force in our calculations, since it is a significant factor for weak events (Lin 2004; Reeves & Forbes 2005b). The physical parameters for the cases we consider here are as follows:

$$M_A = 0.025, \quad h_0 = 2 \times 10^9 \text{ cm},$$

$$m = 2.1 \times 10^{16} \text{ g}, \quad \rho = 1.67 \times 10^{-16} \text{ g cm},^{-3}$$

$$\ell = 10^{10} \text{ cm},$$

where m is the mass of the flux rope, ρ is the atmospheric density at the base of the corona, ℓ is the length of the flux rope, and h_0 is the height of the flux rope at the maximum current point on the equilibrium curve, a convenient normalization point (see Lin & Forbes 2000); M_A is the inflow Alfvén Mach number, which specifies the reconnection rate, and it is fixed at the midpoint of the current sheet. The value chosen for M_A is based on values inferred from observations (e.g., Poletto & Kopp 1986; Yokoyama et al. 2001). We do not vary M_A in this study, since the effects of varying this parameter have been considered previously in Reeves & Forbes (2005a) and Reeves (2006). Our model also requires a value for the background magnetic field strength, given by $A_0/(\pi h_0)$, where A_0 is the surface source flux. We will use values of 25 and 50 G in order to compare flares of different strengths. Details on the relationship between background magnetic field strength and flare intensity in this model can also be found in Reeves & Forbes (2005a).

3. HYDRODYNAMIC LOOP MODEL

To compute the response of the solar atmosphere to the energy released during reconnection we solve the one-dimensional hydrodynamic equations using the Solar Flux Tube Model (SOLFTM) code developed at the Naval Research Laboratory (e.g., Mariska 1987). It solves the equations of mass, momentum, and energy conservation given by

$$\frac{\partial \rho}{\partial t} + \frac{\partial}{\partial s}(\rho v) = 0, \tag{1}$$

$$\frac{\partial}{\partial t}(\rho v) + \frac{\partial}{\partial s}(\rho v^2) = -\rho g - \frac{\partial P}{\partial s}, \tag{2}$$

$$\frac{\partial E}{\partial t} + \frac{\partial}{\partial s}\left[(E+P)v - \kappa \frac{\partial T}{\partial s}\right] = -\rho v g - P_{\text{rad}} + \epsilon, \tag{3}$$

where the energy, E, is the combination of the kinetic and internal energy, given by

$$E = \frac{1}{2}\rho v^2 + \frac{P}{\gamma - 1}. \tag{4}$$

In the above equations, t is time, s is the distance along the loop, ρ is the density, v is the velocity, P is the pressure, g is the acceleration due to gravity, κ is the thermal conductivity coefficient along a field line, T is the temperature, P_{rad} is the energy loss due

to radiation, ϵ is the heating rate, and γ is the ratio of specific heats, taken to be 5/3. For simplicity, the loops are assumed to be semicircular with a constant cross-sectional area, and they are oriented perpendicularly to the Sun's surface. In actuality, the loops are cusp-shaped near the apex of the flare loop system, and have only an approximately circular shape at lower heights. The error introduced in the loop length, L, by not including the exact shape is about 20% for loops near the apex and 2%–3% for loops near the surface (Forbes & Acton 1996).

The loops in the SOLFTM code are made up of chromospheric, transition region, and coronal segments. The chromospheric region of the loop consists of a reservoir of mass in hydrostatic equilibrium at 10^4 K. The spatial resolution along a loop is variable, with many small grid points in the transition region, where the properties of the plasma in the loop change rapidly along the loop. This high-resolution grid moves so that it is always centered on the peak temperature gradient. The initial state of each loop in the code is as a loop in hydrostatic equilibrium with an apex temperature of 1 MK. There are symmetric boundary conditions at the loop top, so that the velocity is zero at the top of the loop, and the gradients of the density and temperature vanish there.

We construct an arcade consisting of 140 discrete loops, with a new loop appearing every 20 s, allowing us to follow the evolution of the flare from the rise phase for several hours with a time resolution of about 20 s. The input heating rate in each loop is given by

$$\epsilon(s, t) = \epsilon_0 + f(s)g(t)\epsilon_{\text{flare}}, \tag{5}$$

where ϵ_0 is the background heating parameter. We choose $g(t)$ to be a triangular function and $f(s)$ to be a Gaussian function given by $\exp[-(s - s_0)^2/2\sigma^2]$, where s_0 is the apex of the loop, σ is the width of the heating region (taken to be 10^8 cm), and ϵ_{flare} is the constant amplitude of the heating. These functional forms are the same as those used in Warren (2006), except that we use a width of 40 s for the width of the triangular heating function, as opposed to a width of 200 s used in Warren (2006). We use a narrower heating window because we assume that an individual field line is heated only as it passes through the reconnection region. The speed of the reconnection outflow is between 10^3 and 10^4 km s^{-1} early on in the eruption. At these speeds it only takes $1-10$ s for the field line to travel through a reconnection region that is 10^4 km long. From this perspective, an even narrower heating window (e.g., 1 s) could be used, but such a short heating duration would entail excessive computing times in the numerical calculations, and there is evidence that a short heating window leads to simulated flare temperatures that are higher than observations (Warren 2006). We thus choose a heating window that is on the narrow side, but that is wider than the 20 s window that caused elevated temperatures in the Warren (2006) study.

The total energy in the loop is related to the input flare heating rate by

$$\epsilon_T = A \int_0^L \int_0^{\Delta t} f(s)g(t)\epsilon_{\text{flare}} \, ds \, dt, \tag{6}$$

where L is the total length of the loop, Δt is the duration of the heating function, and A is the area of the loop, given by the loop thickness times the length of the arcade. The loop length is determined by tracing the length of a field line in the magnetic structure output by the loss-of-equilibrium model. The thickness of each loop is taken to be the distance between adjacent field lines.

The total energy input into each loop is calculated by integrating half of the Poynting flux from the loss-of-equilibrium
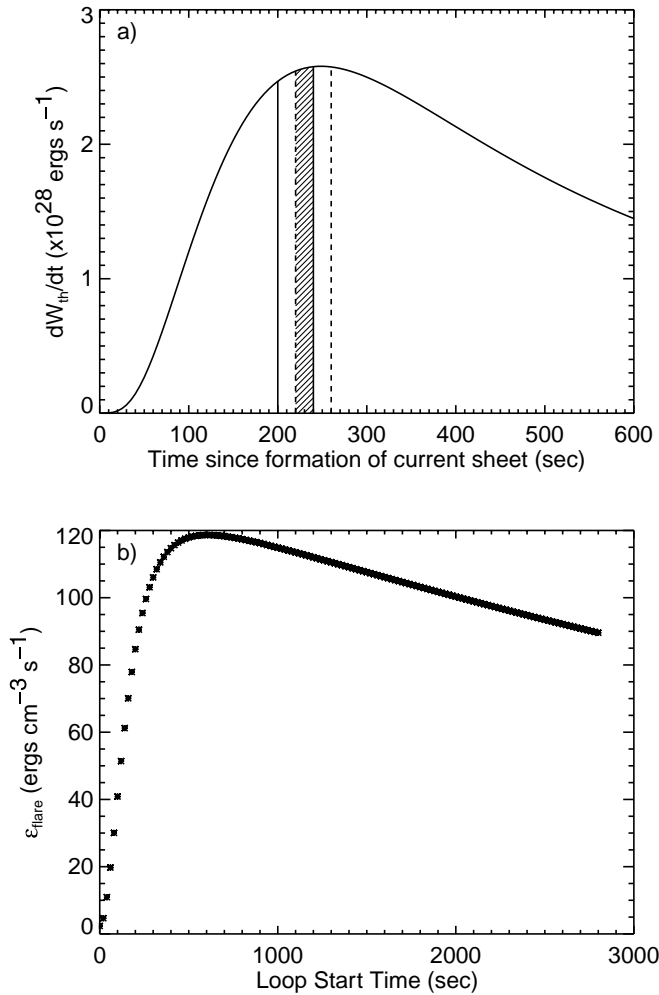
FIG. 2.—(*a*) Plot of the energy release rate from the loss-of-equilibrium calculation. Solid and dashed vertical lines indicate the start and end times for the 10th and 11th loops, respectively, in the calculation. The shaded area indicates the times where there is overlap between the two loops. (*b*) Calculated $\epsilon_{\mathrm{flare}}$ input into each loop. In this case, $B_0 = 50$ G.

calculation over the duration of the heating and dividing by an additional factor of 2. This factor comes about because the heating envelope is 40 s wide, but new loops are formed every 20 s, so there is overlap of the heating windows (see Fig. 2*a*). Once ϵ_T has been determined, we use equation (6) to solve for $\epsilon_{\mathrm{flare}}$ using the functions for $f(s)$ and $g(t)$ given above. The values of $\epsilon_{\mathrm{flare}}$ calculated for each loop are plotted in Figure 2*b*.

Figure 3 shows the evolution of one of the loops in the simulation (loop 30). The background magnetic field in this case is 50 G. In the first phase of the evolution, shown in the left-hand column of Figure 3, thermal energy is conducted along the loop into the chromosphere, which heats up. The enhanced pressure causes a weak shock front (with Mach numbers between 1.2 and 1.4) to form. Expansion of the plasma in the chromosphere also causes a downward velocity near the base of the loop, which is a characteristic feature of explosive evaporation (Fisher et al. 1985a). The temperature in the loop reaches its maximum value as the shock front is about halfway up the leg of the loop, and then begins to decrease.

Since the boundary conditions at the top of the loop are symmetric, a density enhancement occurs when the shocks from each leg of the loop meet at the loop top and pass each other. Equivalently, one may think of this process as a reflection of the shock.

The density enhancement then travels back down the loop to the chromosphere, as shown in the center column in Figure 3, while the temperature of the loop continues to decrease.

When the reflected shock reaches the chromosphere, a secondary evaporation of material takes place. This phase is shown in the right-hand column in Figure 3. This density enhancement is more gentle than that caused by the initial shock front in the initial phase of evolution. When the enhancement reaches the top of the loop, it is added to the enhancement generated in the other leg of the loop, just as before. This process can repeat more than once, leading to multiple evaporation events in some loops, although each event is progressively weaker.

The temperature and density evolution for the entire arcade of 140 loops is shown in Figure 4. The evolution of the temperature, shown in the top panels of Figure 4, shows that there is a high temperature region of about 25 MK at the top of the arcade. The rest of the loops in the arcade have undergone some cooling, and the bulk of the plasma is at about 5 MK. This temperature structure is consistent with observations of flares that show hot regions of plasma at the top of the flare arcade (e.g., Tsuneta et al. 1997; Warren & Reeves 2001). The evolution of the density, shown in the bottom panels of Figure 4, shows the evaporation and subsequent density enhancement that takes place when the shock wave reaches the tops of the loops in the SOLFTM calculation. Bands of high density form in the arcade as loops evolve through the multiple evaporation stages at different times. The density in the loops begins to rise at the feet, just before the top of the chromosphere, for all of the loops in the arcade.

4. FLARE IMAGES AND LIGHT CURVES

In this section we use the results of our multithreaded hydrodynamic flare calculation discussed in the previous section to construct flare light curves for the *GOES* 1–8 Å flux band, and images SXT on *Yohkoh* and *TRACE*. The *GOES* instrument is a full-Sun X-ray flux monitor (see Kahler & Kreplin [1991] for instrumentation details), and the peak flux in the *GOES* 1–8 Å band during a flare is used to classify the event. The SXT instrument on *Yohkoh* has a variety of broadband filters that allows the telescope to view plasma at a broad range of temperatures (Tsuneta et al. 1991). We will focus on three of these filters: the Be119 filter, which is sensitive to plasma temperatures of >10 MK; the Al12 filter, which is sensitive to plasmas around 10 MK; and the Al.1 filter, which is sensitive to plasmas below 5 MK. *TRACE* is a narrowband imaging telescope that detects wavelengths in the extreme ultraviolet (Handy et al. 1999). The 195 Å filter is mostly sensitive to emission from Fe XII at 1.5 MK, although there is also some emission in this wave band from Fe XXIV, which has a formation temperature of about 20 MK. The 171 Å band is only sensitive to emission from Fe IX and Fe X at 1 MK.

Figure 5 shows the *GOES* light curves for simulations with background magnetic field strengths of 25 and 50 G. The 25 G background field case, shown in Figure 5*a*, corresponds to a B2.5 flare in the GOES flare classification scheme. The 50 G background magnetic field case, shown in Figure 5*b*, is an M1.0 flare. The flare light curves are similar in shape, except that the light curve for the stronger flare has a faster rise time and peaks earlier than the weaker flare light curve. This result is not surprising, given that the thermal energy release rate in the loss-of-equilibrium model rises faster and peaks earlier when the background magnetic field is stronger (Reeves & Forbes 2005a).

Figure 6 shows a series of images for the simulation with the 50 G background magnetic field (M1.0 flare) in the *TRACE* 195 and 171 Å passbands. Early in the flare, bright footpoint emission
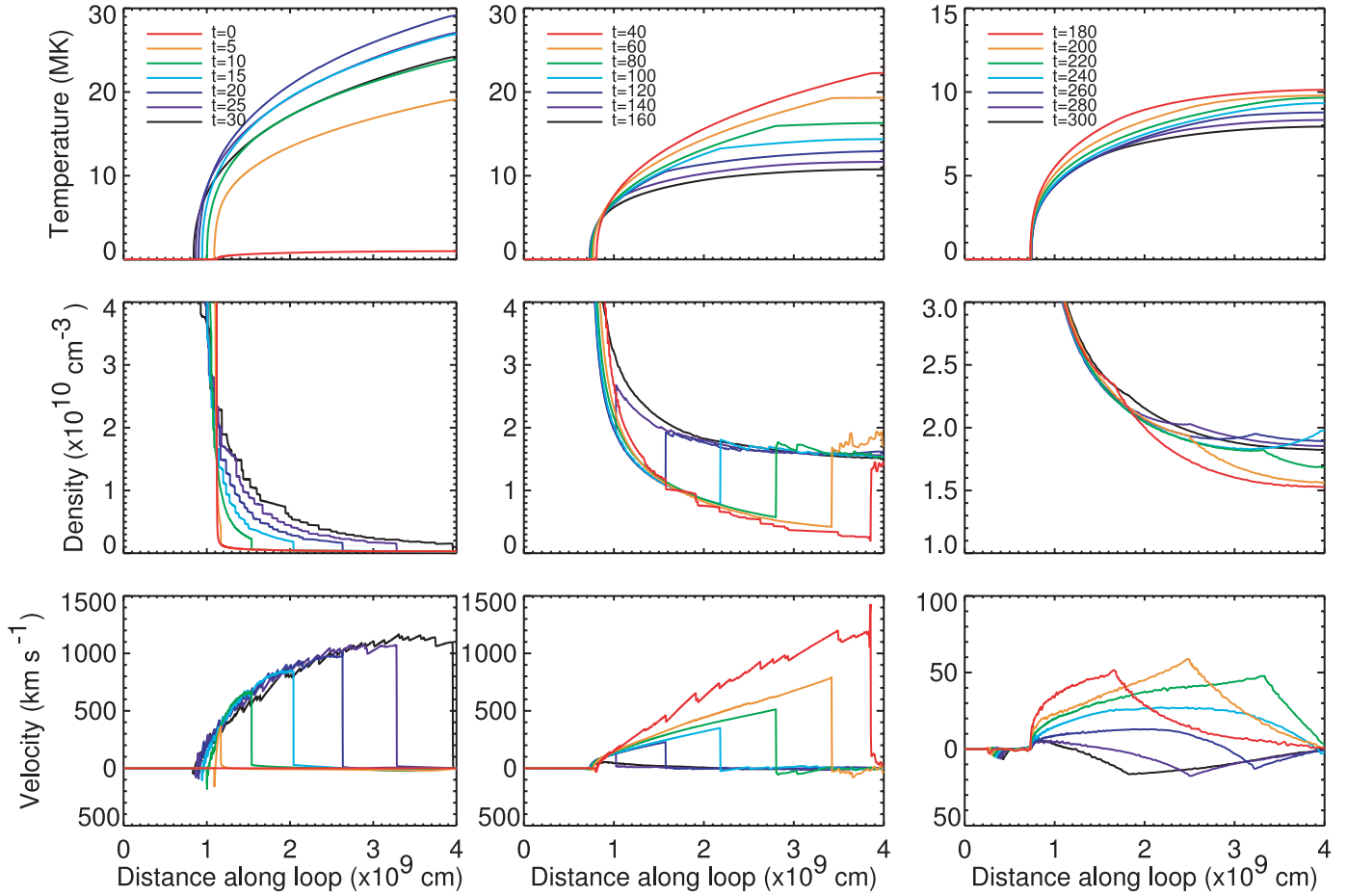
FIG. 3.—Plot of the evolution of the temperature (*top*), density (*middle*), and velocity (*bottom*) as a function of loop length for loop 30. The leftmost column shows the loop during the evaporation phase of the hydrodynamic simulation, the center column shows the loop during the reverse shock phase, and the rightmost column shows the loop during the secondary evaporation phase. In this case, $B_0 = 50$ G.
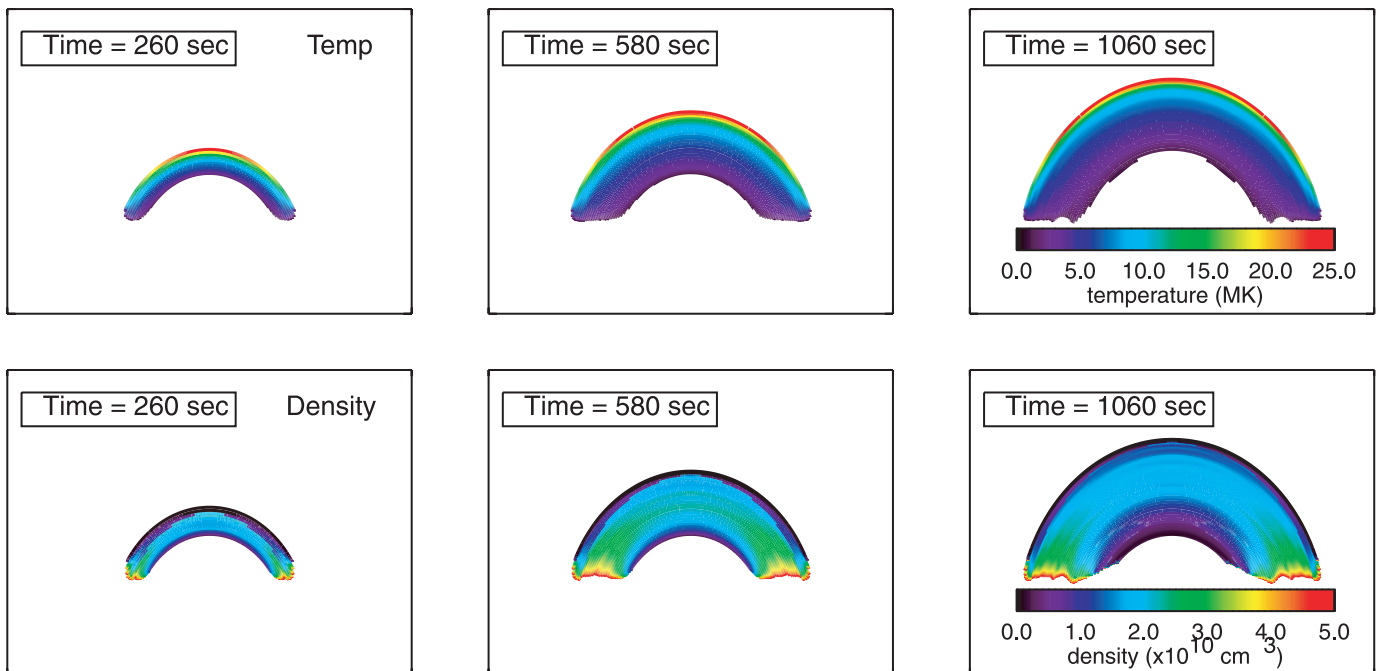

FIG. 4.—Evolution of the simulated flare temperature (*top*) and density (*bottom*) for the entire flare arcade. In this case, $B_0 = 50$ G.
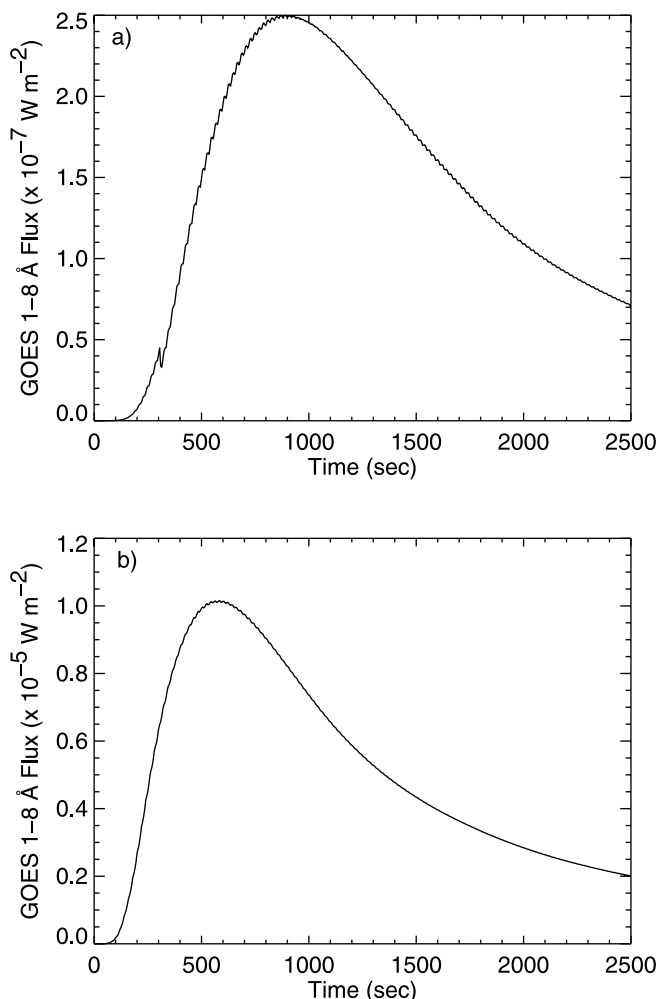
FIG. 5.—*GOES* light curves for the cases with a background field of (*a*) 25 G and (*b*) 50 G. The small-amplitude oscillations are due to the discretization of the flare loop system.

is seen in both passbands, and some loop-top emission is visible in the 195 Å passband. There is no corresponding loop-top emission enhancement in the 171 Å passband. A similar loop-top emission is often observed in 195 Å images of solar flares manifesting as a barlike bright structure at the top of flare arcades (Warren 2000). Accompanying observations with the 171 Å filter show no such structure. This phenomenon is due to the sensitivity of the 195 Å bandpass to Fe xxiv, which is formed at around 20 MK. The 171 Å passband has very little sensitivity at hot temperatures, and generally only images broadband continuum at these temperatures.

Figure 7 shows the evolution of intensity of the arcade in the SXT Be119, Al12, and Al.1 filters. In all of the filters, there is an intensity enhancement at the top of the arcade that remains as the flare evolves. A similar bright knot is often seen in flares observed with SXT (Feldman et al. 1994; Doschek et al. 1995; Doschek & Warren 2005), although for a better comparison, we would need to include the cusp geometry of the loops as well as projection effects (see Forbes & Acton 1996). The maximum value of the SXT intensity in the loop-top sources in our calculations is approximately 10 times the intensity in the legs of the loop, which is consistent with the observed properties of these features (Feldman et al. 1995b).

The bright structure that appears at the top of the arcade in our simulations has a banded structure due to the multiple evaporative phases that occur in each loop. The bright intensity at the very top

of the arcade occurs when the first front of dense, hot plasma reaches the loop top. Subsequent bands of bright intensity are due to the weaker evaporative fronts reaching the tops of loops that have reached the secondary evaporative phases.

One-dimensional flare simulations consisting of a single loop are unable to reproduce this sustained bright emission in the top of the loop, because the high pressure needed to confine the plasma there cannot be sustained for more than a few wave transit times. However, in our calculation there are many loops in different stages of evolution, and because new loops are constantly being created and energized, there are always loops near the top that are entering the reverse shock phase of the evolution and have enhanced densities, causing the persistent bright loop-top emission.

The regions of high intensity in the multibanded structure are only about 1″ wide in this case. Images obtained by SXT, which has a resolution of 2.5″, cannot resolve this fine structure. Figure 8 shows the simulated Be119 image at 580 s rebinned to the resolution of SXT. With this resolution, the two brightest intensity bands become one bright knot at the top of the loop. Figure 8 also shows the same image, rebinned to the resolution (1″ pixels) of the X-Ray Telescope (XRT) on the *Hinode* (*Solar B*) satellite. In this image, the two brightest intensity bands are just barely resolvable. Thus it is quite possible that XRT will be the first instrument to observe in detail features that can be directly attributed to shock waves traveling back and forth in the newly formed flare loops.

Earlier simulations using multithreaded hydrodynamic simulations performed by Hori et al. (1997) were able to reproduce the bright loop-top knot in the Be119 filter, but not in the Al.1 filter, probably because by the time the loops cooled enough to be seen by the Al.1 filter, the pressure in the loops has more or less equalized. In our simulations, there are several echoes of the wave front associated with the onset of chromospheric evaporation (see Fig. 3), so a loop-top pressure enhancement persists even after the loops have cooled to lower temperatures.

5. SIMULATED FLARE SPECTRA AND BLUESHIFTS

In this section we use the results of our multithread hydrodynamic simulation using the SOLFTM code to calculate synthetic spectra for the Bragg Crystal Spectrometer (BCS) on *Yohkoh* (Culhane et al. 1991). BCS consists of several spectrometers observing the emission lines S xv, Ca xix, Fe xxv, and Fe xxvi. The Fe xxvi line is not often used due to detector problems (e.g., Warren & Doschek 2005). The S xv, Ca xix, and Fe xxv lines have peak responses at about 14, 25, and 52 MK, respectively (Feldman et al. 1996b). The Ca xix line has the best spectral resolution, and is often employed in flare simulations and observational analysis (Doschek & Warren 2005), so this line will be the primary focus of this section. The BCS spectrometers are uncollimated, so that they observe emission from the entirety of the Sun's disk.

The simulated spectra are derived from the multithread SOLFTM model as follows: for each thread, the temperature and the normal component of the velocity (assuming that the line of sight is perpendicular to the chromosphere) in each cell are passed to the `bcs_spec` routine (which is part of the standard SolarSoft package for analyzing BCS data). This routine computes spectra at the wavelengths observed by BCS for plasma given an input temperature and velocity. The resulting spectra from each cell are added to give a composite spectrum for each thread. Then spectra from all of the threads are added, keeping in mind that each loop is created and energized at a different time as the reconnection site progresses upward. Because of the rising reconnection site, the loops that make up the arcade and contribute to the total spectrum will each be at different points in their evolution.

171Å

Time = 260 sec   195Å
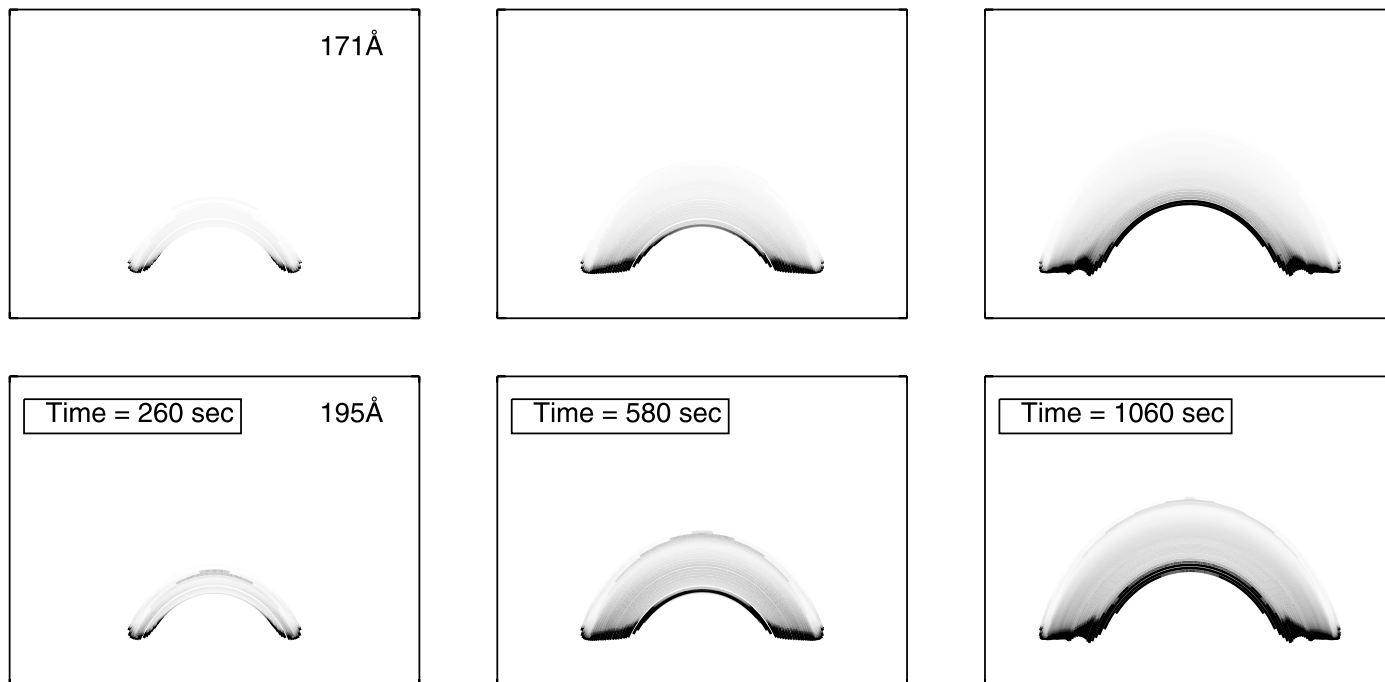
Time = 580 sec

Time = 1060 sec

FIG. 6.—Simulated intensities for *TRACE* 171 Å (*top*) and 195 Å (*bottom*) filters. The color table is reversed, so that dark shading indicates high intensities.

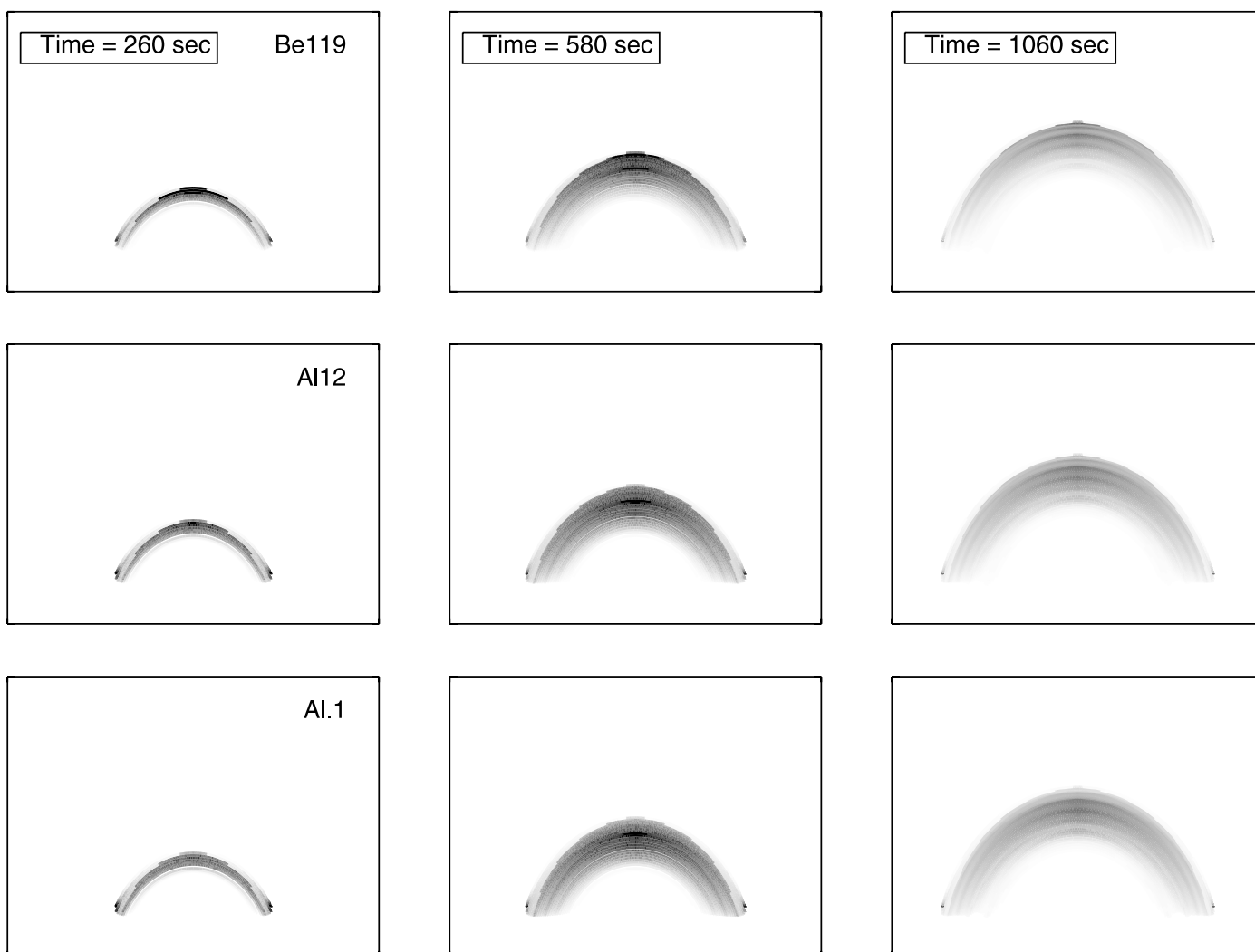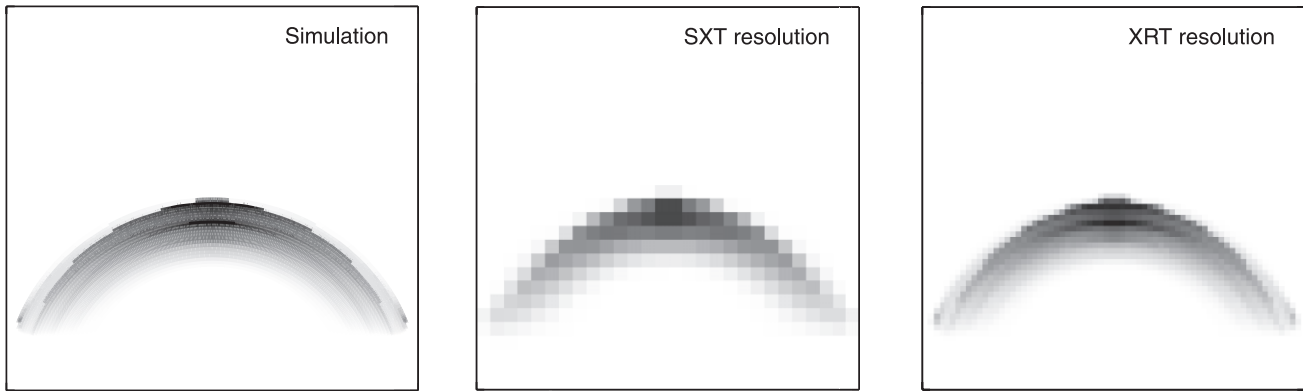Time = 260 sec   Be119

Time = 580 sec

Time = 1060 sec

Al12

Al.1

FIG. 7.—Simulated SXT intensities for the Be119 (*top*), Al12 (*middle*), and Al.1 (*bottom*) filters. The color table is reversed, so that dark shading indicates high intensities.

FIG. 8.—Simulated images of a flare loop system, as seen through the SXT Be119 filter. The panel on the left is unbinned, the panel in the center is scaled to the spatial resolution of the *Yohkoh* SXT, and the panel on the right is scaled to the resolution of the XRT on *Hinode* (*Solar B*).

A common way of determining the temperature of a solar flare is to measure the spectrum of a He-like ion at the time of peak emission and determine the temperature by finding the ratio of dielectric recombination satellite lines to the resonance line (e.g., Phillips & Feldman 1995; Feldman et al. 1995a, 1996a, 1996b). This method gives a response-weighted average temperature for the flare, since the emission from many different loops in the observed arcade will contribute to the spectrum. With BCS, the Fe xxv line is often used for high-intensity flares like the M1.0 flare we are simulating (Feldman et al. 1995a), and either the S xv or the Ca xix line is used for cooler flares (Phillips & Feldman 1995; Feldman et al. 1996b).

The average temperature of the bulk plasma in solar flares can be determined by fitting a synthetic BCS spectrum created using the bcs_spec routine to the observed spectrum. We vary the temperature input to bcs_spec, assuming no velocity, until we find a spectrum that best matches the one generated by our multithread model. Figure 9a shows the Ca xix spectrum of the simulated B2.5 flare at the time of maximum emission in the Ca xix band, and a synthetic spectrum generated by bcs_spec at 8 MK. Figure 9b shows a similar plot of the Fe xxv spectrum for the M1.0 flare, along with a synthetic spectrum generated at 17 MK. Even though the flares generated by our model consist of many loops containing flowing plasma at different temperatures, the spectra they generate are roughly similar to the single-temperature, stationary spectra generated by bcs_spec. Given this result, it is easy to see why flares were originally thought to be reasonably well modeled using only a single loop.

Feldman et al. (1996b) performed a comprehensive study of the correlation between *GOES* flare class and temperature as measured by BCS. They find that there is a linear relationship between X-ray flare class and BCS temperature. Figure 10 shows the data from Feldman et al. (1996b) with the data from our two simulated flares superimposed. The temperatures found by matching the output of bcs_spec to spectra generated by our model are within the spread of data points presented by Feldman et al. (1996b), and thus the correlation between the BCS temperature and X-ray flare class in the two simulated flares agrees with observations. Although there are numerous factors and complex calculations that go into determining the flare class and temperature, the overall correlation can be understood as a consequence of the fact that the flare class and the flare temperature are both functions of the magnetic energy density processed through the current sheet. The flare magnitude, however, also depends on the volume of the flare, which we have assumed to be the same in our two cases.
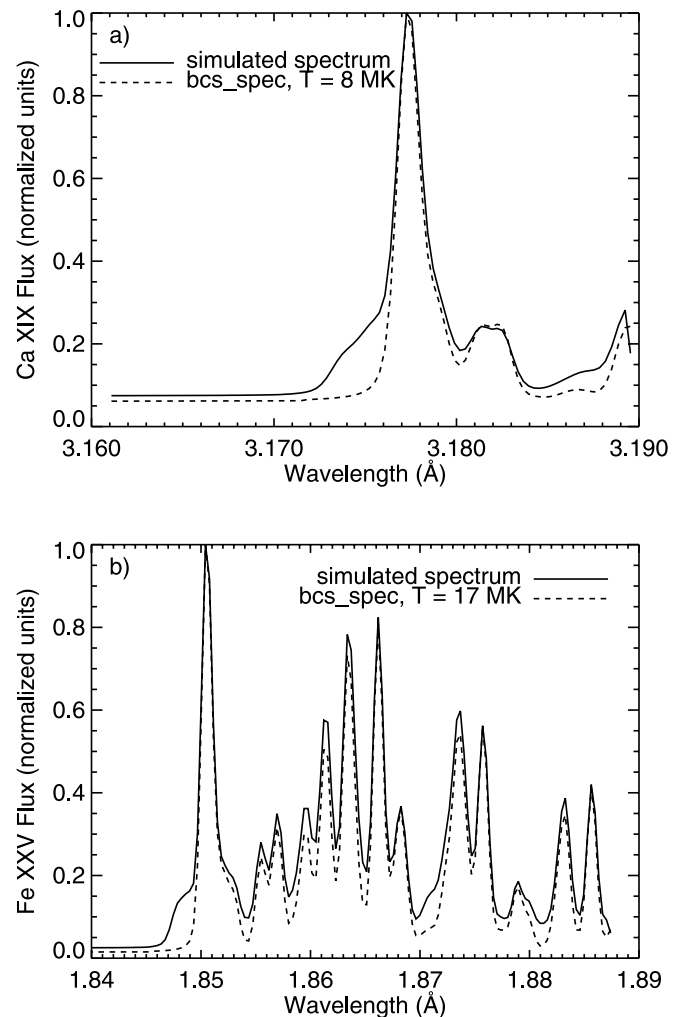

FIG. 9.— (*a*) Ca xix spectrum at the time of peak emission from the hydrodynamic simulation for the B2.5 flare (*solid line*) and a synthetic spectrum calculated using bcs_spec for a stationary plasma with a temperature of 8 MK. (*b*) Fe xxv spectrum at the time of peak emission from the hydrodynamic simulation for the M1.0 flare (*solid line*) and a synthetic spectrum calculated using bcs – spec for a stationary plasma with a temperature of 17 MK.
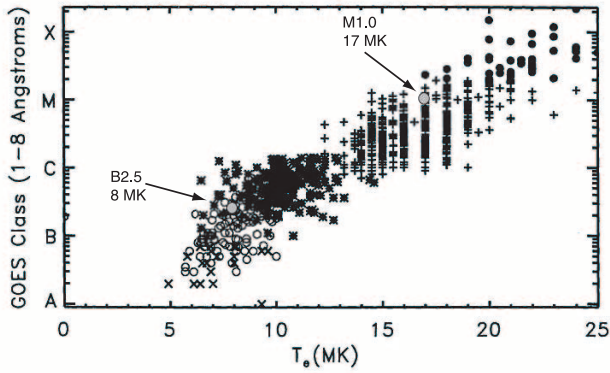
FIG. 10.—Data from Feldman et al. (1996b) correlating *GOES* class and BCS temperature. The data from our two model flares are overlaid as gray circles. The black circles are flares with *GOES* class M2 and higher, which saturate the BCS detectors. Other symbols indicate original papers from which the data were collected (see Feldman et al. 1996b for details).

FIG. 11.—Plot of BCS Ca XIX light curve (*top*) and spectra from several different times (*bottom*). The times are when the light curve is at: peak flux (*diamond and solid line*), 25 photons cm^{-2} s^{-1} (*triangle and dotted line*), and 3.5 photons cm^{-2} s^{-1} (*asterisk and dashed line*). The vertical line in the bottom panel marks the rest wavelength of the resonance line.

The differences in volume of observed flares may account for the scatter in the observational data presented in Feldman et al. (1996b) and Figure 10.

Most observed flare spectra are dominated by an unshifted resonance line due to stationary plasma in the flare loops. An isolated blueshifted spectral component that would result from chromospheric evaporation in a single loop is rarely observed by full-Sun spectrometers such as BCS. Typically, what is observed is a blue wing on the stationary component, and often no blue wing is observed at all. Some authors have speculated that blueshifted spectral features are not observed early in the flare evolution because the instruments used to measure the spectra are not sensitive enough (e.g., Antonucci et al. 1987; Doschek & Warren 2005). Examining the simulated flare spectra allows us to investigate this claim and determine the instrumental sensitivity needed to observe blueshifts caused by chromospheric evaporation.

Figure 11 shows the light curve for the Ca XIX line for the simulated M1.0 flare. Also shown are simulated flare spectra taken at several different times along the light curve. Doschek & Warren (2005) have determined that the first detectable spectrum in the BCS Ca XIX line occurs when there are about 25 photons cm^{-2} s^{-1} total emission in the light curve. The dotted line in Figure 11 (*bottom*) is the simulated spectrum at the time when the light curve is at this level. There is a blueshifted wing to this spectrum, but the stationary component is more prominent. The dashed line is a spectrum at the time when there are 3.5 photons cm^{-2} s^{-1} total emission in the light curve, and in this spectrum, the blueshifted component dominates the emission. Thus in this simulation, the strong blueshifts early in the flare evolution occur below the sensitivity threshold of the BCS instrument, and are therefore undetectable, as Antonucci et al. (1987) and Doschek & Warren (2005) have argued. The solid line in Figure 11 (*bottom*) shows the Ca XIX spectrum at the time of peak emission in that line. At this time, the spectrum is totally dominated by the stationary component, and the line width is much narrower than the earlier spectra.

Figure 12 shows each of the spectra presented in Figure 11 (*bottom*), along with the spectra of the individual loops that contribute to the total spectrum. Figure 12*a* shows the spectrum early in the flare, before there is enough emission for it to be detected by BCS. There are only a few loops contributing to this spectrum, and the greatest contribution comes from the one loop where chromospheric evaporation is occurring, causing the resonance line to be shifted toward bluer wavelengths. Figure 12*b* shows the spec-
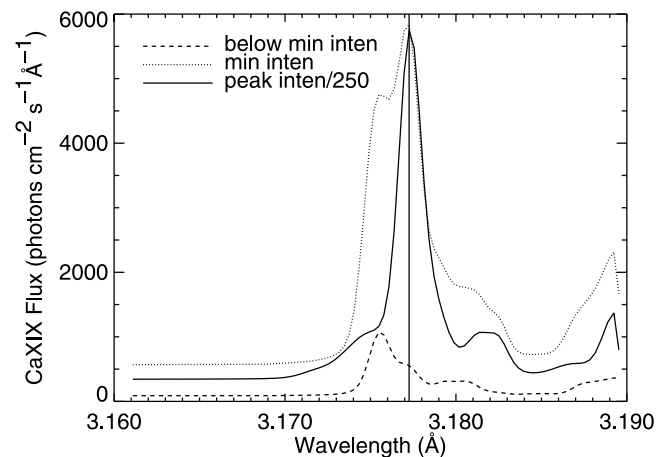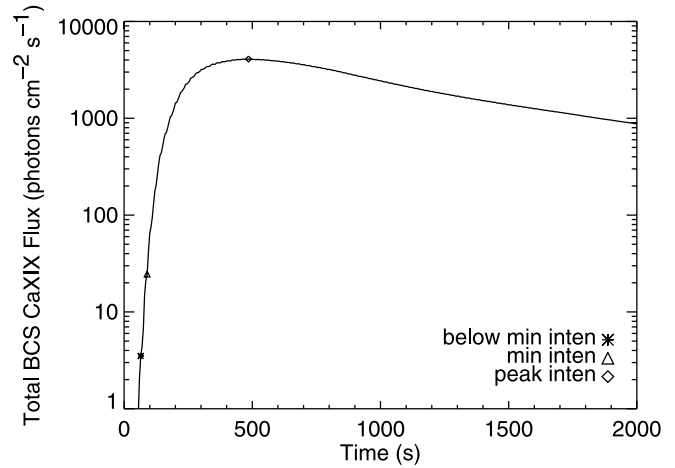
trum at the time when the emission is at the minimum detectable level for the BCS instrument. There is still a loop that is undergoing chromospheric evaporation, but by this time, the plasma in the loops formed previously has stopped flowing, and the emission from these loops gives rise to the stationary component in the spectrum. By the time the Ca XIX emission reaches its peak, shown in Figure 12*c*, the plasma in the majority of the loops has stopped moving, so that the stationary component is very strong and newly created loops containing evaporating plasma do not contribute much to the total spectrum.

In their multiloop hydrodynamic calculations, Hori et al. (1998) used a fixed amount of heat flux in each loop that is based on an estimate of the total energy released in a typical flare. They found that in order to reproduce spectral observations using this heat input, the heating duration, $\tau_{\rm heat}$, must be less than the time required for evaporated plasma to fill the loop, τ_c, for loops formed in the early stages of the flare, but $\tau_{\rm heat}$ must be greater than τ_c for loops formed during the later stages of flare evolution. The heating flux in our simulations (Fig. 2*b*) is derived from a calculation of the thermal energy released by reconnecting magnetic fields in the current sheet formed above the flare, and thus in our model, loops in the early stages of the flare are heated less than loops that are formed later in the flare evolution. We have also made the heating duration and shape of the heating window as consistent as possible
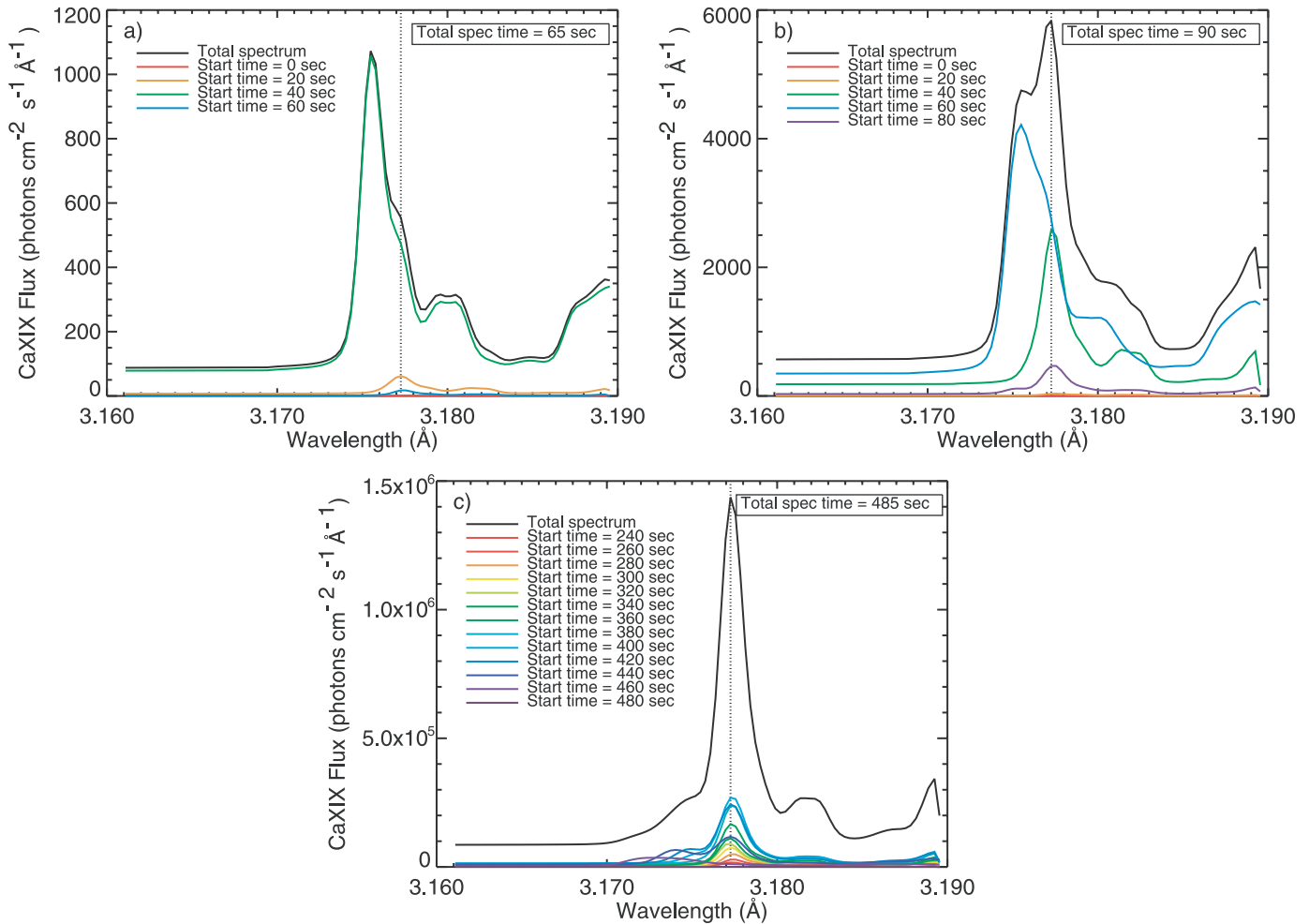
FIG. 12.—Plots of total spectra and spectral contributions of individual loops for the three different spectra shown in Fig. 11 (*bottom*). The vertical lines mark the rest wavelength of the resonance line.

(within the confines of the numerical model) with the physical picture of continuously reconnecting magnetic fields. Using this model-derived function for the heat flux into the loops, we are able to naturally reproduce observed flare spectra without the need to tune the parameters of the heating function.

6. SUMMARY AND DISCUSSION

In this paper, we present a model of flare evolution that integrates a model of the reconnection process with a multistranded hydrodynamic flare loop simulation, thus generating the heat input into the simulated flare loops from first principles. This model follows the evolution of the flare from the onset to the late phase, and it includes the effects of chromospheric evaporation and radiative and conductive cooling. We have simulated flare emissions for a variety of instruments using this model, and we have found that the results of these simulations are consistent with the properties of observed flares.

In our simulations, we are able to reproduce loop-top knots of bright emission that are often seen in SXT. It has been suggested by some authors (e.g., Feldman et al. 1994; Doschek & Warren 2005) that these knots present a problem for hydrodynamic flare models, since they provide no forces that would confine plasma in the tops of the loops. However, our multithread hydrodynamic simulation naturally produces an arcade with a persistent high-intensity loop-top knot without the need to introduce any new forces outside the scope of hydrodynamics. This intensity enhance-

ment is the result of density fronts colliding at the top of each loop, and it persists because new loops are continually being formed and undergoing chromospheric evaporation, so that there are always loops with colliding density fronts at the top of the multi-threaded arcade.

The loop-top intensity enhancement predicted by our model is multibanded because of the multistage evaporative process that the loops go through. This banded structure is below the spatial resolution of current instrumentation, but future missions, such as the X-ray Telescope (XRT) on *Hinode* (*Solar B*), may be able to resolve it. Thus we have shown that the spatial structure of the loop-top intensity can, in principle, provide information about the evaporative physics in the flare arcade.

We have also used our model to simulate flare spectra, and we have found that our model reproduces the expected observational signatures quite well. We find that the coupling of the energy release rates from the loss-of-equilibrium calculation with the hydrodynamic code for the flaring plasma gives reasonable light curves and spectra in BCS. We calculate the emission measure–weighted average temperatures at peak emission for two very different size flares, a B2.5 flare and an M1.0 flare, and find that they fall within the range of observed values.

We use the calculated spectra to understand why the blue-shifts predicted by the theory of chromospheric evaporation are not routinely observed with BCS. We examine spectra from the Ca XIX line for the M1 flare, and find that there is already a

REEVES, WARREN, & FORBES

stationary component to the spectrum at the time when there are just enough counts for BCS to collect meaningful spectra. Earlier than this time, our simulated spectra show dramatic blueshifts. Such blueshifts have been observed near flare ribbons by the *SOHO* CDS imaging spectrometer during the decay phase (Czaykowska et al. 1999), and more recently during the flare impulsive phase (Brosius & Phillips 2004; Milligan et al. 2006). Our model predicts that these blueshifts should always be present, and they should be observed even more often in the future by more sensitive instruments, such as the EUV Imaging Spectrometer (EIS) on *Hinode* (*Solar B*), launched in 2006 September.

Our model differs from previous multistranded flare models because we use the physics of the reconnection process to determine the amount of heating that should go into each loop. Nevertheless, there are still some arbitrary factors that appear in the equation for determining the heat input into each thread in our model, such as the shape of the heating function in space and time in each loop, and the duration of the heating. We have chosen the duration of the heating to be short so as to be as consistent as possible with the physical processes that we are modeling, taking into account the constraints of the numerical code. Warren (2006) has shown that a narrow heating window can lead to elevated temperatures in the simulation; however, so in order to verify that our conclusions remain valid with a wider heating window, we have repeated the M1.0 flare simulation with a heating duration of 200 s. Although this heating window is somewhat wide given our physical picture, it serves as an upper limit to determine how sensitive our results are with respect to the heating window width. In this case we find that there are still blueshifts in the Ca xix spectra at very early times, but they are at lower emission levels than in the simulation with a 40 s heating window, since in the case of the

200 s heating window the evaporation in the loops is more gentle. In addition, the simulated SXT Al12 filter images in the case with a 200 s heating window have a multiple banded structure similar to the images constructed from the case with the 40 s heating window. However, the simulated Be119 filter images in the case with a 200 s heating window do not have multiple bands of intensity. In the case with the 200 s heating window, there are still multiple evaporation events, but they happen more slowly, so that by the time that the second evaporation occurs, the plasma has cooled out of the range where the Be119 filter is the most sensitive. These results show that future high spatial resolution observations of flares with EIS and XRT on *Hinode* (*Solar B*) may be able to offer information about the heating timescale of the flare loops.

Although we have not attempted to reproduce a specific event, the results from this cradle-to-grave flare evolution model compare very favorably to observed flare characteristics. Thus we conclude that the reconnection model is energetically consistent with observed flare emissions.

REFERENCES

Antonucci, E., Dodero, M. A., & Martin, R. 1990, ApJS, 73, 137
Antonucci, E., Dodero, M. A., Peres, G., Serio, S., & Rosner, R. 1987, ApJ, 322, 522
Bentley, R. D., Doschek, G. A., Simnett, G. M., Rilee, M. L., Mariska, J. T., Culhane, J. L., Kosugi, T., & Watanabe, T. 1994, ApJ, 421, L55
Brosius, J. W., & Phillips, K. J. H. 2004, ApJ, 613, 580
Cheng, C.-C., Oran, E. S., Doschek, G. A., Boris, J. P., & Mariska, J. T. 1983, ApJ, 265, 1090
Culhane, J. L., et al. 1991, Sol. Phys., 136, 89
Czaykowska, A., de Pontieu, B., Alexander, D., & Rank, G. 1999, ApJ, 521, L75
Doschek, G. A., Cheng, C. C., Oran, E. S., Boris, J. P., & Mariska, J. T. 1983, ApJ, 265, 1103
Doschek, G. A., Strong, K. T., & Tsuneta, S. 1995, ApJ, 440, 370
Doschek, G. A., & Warren, H. P. 2005, ApJ, 629, 1150
Doschek, G. A., et al. 1994, ApJ, 431, 888
Feldman, U., Doschek, G. A., & Behring, W. E. 1996a, ApJ, 461, 465
Feldman, U., Doschek, G. A., Behring, W. E., & Phillips, K. J. H. 1996b, ApJ, 460, 1034
Feldman, U., Doschek, G. A., Mariska, J. T., & Brown, C. M. 1995a, ApJ, 450, 441
Feldman, U., Seely, J. F., Doschek, G. A., Brown, C. M., Phillips, K. J. H., & Lang, J. 1995b, ApJ, 446, 860
Feldman, U., Seely, J. F., Doschek, G. A., Strong, K. T., Acton, L. W., Uchida, Y., & Tsuneta, S. 1994, ApJ, 424, 444
Fisher, G. H., Canfield, R. C., & McClymont, A. N. 1985a, ApJ, 289, 434
———. 1985b, ApJ, 289, 425
Forbes, T. G., & Acton, L. W. 1996, ApJ, 459, 330
Handy, B. N., et al. 1999, Sol. Phys., 187, 229

Hori, K., Yokoyama, T., Kosugi, T., & Shibata, K. 1997, ApJ, 489, 426
———. 1998, ApJ, 500, 492
Kahler, S. W., & Kreplin, R. W. 1991, Sol. Phys., 133, 371
Lin, J. 2004, Sol. Phys., 219, 169
Lin, J., & Forbes, T. G. 2000, J. Geophys. Res., 105, 2375
Lin, R. P., & Hudson, H. S. 1976, Sol. Phys., 50, 153
Mariska, J. T. 1987, ApJ, 319, 465
Milligan, R. O., Gallagher, P. T., Mathioudakis, M., Bloomfield, D. S., Keenan, F. P., & Schwartz, R. A. 2006, ApJ, 638, L117
Phillips, K. J. H., & Feldman, U. 1995, A&A, 304, 563
Poletto, G., & Kopp, R. A. 1986, in The Lower Atmosphere of Solar Flares: Proceedings of the Solar Maximum Mission Symposium, ed. D. F Neidig (Sunspot: NSO), 453
Reeves, K. K. 2006, ApJ, 644, 592
Reeves, K. K., & Forbes, T. G. 2005a, ApJ, 630, 1133
———. 2005b, in IAU Symp. 226, Coronal and Stellar Mass Ejections, ed. K. Dere, J. Wang, & Y. Yan (Cambridge: Cambridge Univ. Press), 250
Reeves, K. K., & Warren, H. P. 2002, ApJ, 578, 590
Tsuneta, S., Masuda, S., Kosugi, T., & Sato, J. 1997, ApJ, 478, 787
Tsuneta, S., et al. 1991, Sol. Phys., 136, 37
Warren, H. P. 2000, ApJ, 536, L105
———. 2006, ApJ, 637, 522
Warren, H. P., & Doschek, G. A. 2005, ApJ, 618, L157
Warren, H. P., & Reeves, K. K. 2001, ApJ, 554, L103
Yokoyama, T., Akita, K., Morimoto, T., Inoue, K., & Newmark, J. 2001, ApJ, 546, L69